Thermal Modeling With Surrogate Model-Based Optimization of Direct Oil Cooling Heat Transfer Coefficient for HEV Motor

So-Yeon Im, Tae-Gun Lee, Ki-Won Kim, Jin-Cheol Park, Jun-Woo Chin, and Myung-Seop Lim, *Senior Member, IEEE*

***Abstract*—The traction motor in parallel 2 hybrid electric vehicles adopts a cooling method involving automatic transmission fluid (ATF). The scattered ATF directly cools the heat sources of the electric motor. A thermal model based on the lumped parameter network is developed to reflect the direct oil cooling effect. In the developed oil-cooled lumped parameter thermal network (LPTN), the cooling by the ATF acts as a current source. The oil scattered through the motor shaft has high cooling efficiency, but it is difficult to theoretically calculate the nonlinear fluid behavior. Because the flow rate and rotational speed affect the ATF cooling performance, the convective heat transfer coefficient (HTC) of the ATF is reflected in the direct oil cooling thermal model of the traction motor via the proposed correlation process. In this process, a kriging surrogate model-based optimization is performed to determine the convective HTC of the ATF under specific flow and load conditions. The objective function of the optimization is to minimize the difference between the temperature predicted by the thermal model and experimentally measured temperature. As the kriging surrogate model has high prediction accuracy for nonlinear performance, the direct oil-cooled LPTN developed during the optimization process provides a useful thermal model.**

***Index Terms*—Hybrid electric vehicle motor, kriging surrogate model, oil cooling system, optimization, thermal modeling.**

I. Introduction

As THE automotive industry continually develops to achieve higher power densities, the thermal management of powertrains, including transmission and electric motor, is becoming increasingly crucial [1], [2]. The adoption of an appropriate cooling system is key to the thermal management of electric propulsion systems. In particular, a permanent magnet synchronous motor (PMSM) with high efficiency and high torque density requires efficient cooling to prevent demagnetization of the permanent magnets (PMs) and insulation weakening of the windings [3], [4], [5]. Cooling technology is closely related to the performance and size of traction motors. An increase in the temperature of a traction motor without suitable heat dissipation increases the resistance and reduces the residual magnetic flux density of the PM, thereby reducing the motor performance. Moreover, an increase in the heat dissipation area reduces the thermal resistance but increases the size of the motor. Therefore, an efficient cooling system can suppress temperature increases and improve the torque density and durability of traction motors.

Various cooling methods and structures have been studied to achieve effective cooling performance. In [6], the effect of a water-cooling system on a slotless high-speed motor was studied. By using the integrated cooling method reported in [6], instead of conventional water jacket cooling through the housing, the power density can be increased without changing the design of the motor. The effect of a hybrid cooling system that combines standard liquid cooling with a heat pipe to maintain the temperature of a hybrid electric vehicle (HEV) traction motor was studied in [7]. Liang et al. [8] analyzed the impact of the water jacket shape parameters and convective heat transfer coefficient (HTC) and investigated the thermal performance of an in-wheel motor. To improve heat dissipation, inflection points in which the temperature difference is maximum according to the water jacket configuration parameters should be avoided. The fluid flow for each water jacket shape of a mild HEV traction motor was simulated in [9]. The water jacket concept with parallel spiral fins and a dual inlet arrangement exhibited a comparatively high thermal performance. However, the cooling performance of a housing water jacket differs depending on the assembly conditions such as shrink-fit pressure and thermal grease. Moreover, it is difficult to calculate the contact thermal resistance [10], [11]. Additionally, the housing water jacket is relatively ineffective at dissipating heat from the end windings or rotor.

Manuscript received 27 March 2023; revised 23 July 2023; accepted 7 September 2023. Date of publication 11 September 2023; date of current version 18 January 2024. Paper 2023-EMC-0117.R1, presented at the 2022 IEEE Energy Conversion Congress and Exposition, Detroit, MI, USA, Oct. 09–13, and approved for publication in the IEEE Transactions on Industry Applications by the Electric Machines Committee of the IEEE Industry Applications Society [DOI: 10.1109/ECCE50734.2022.9947410]. This work was supported by the National Research Foundation of Korea funded by the Korea Government (MSIT) under Grant RS-2023-00207865. *(Corresponding author: Myung-Seop Lim.)*

So-Yeon Im, Tae-Gun Lee, Ki-Won Kim, and Myung-Seop Lim are with the Department of Automotive Engineering (Automotive-Computer Convergence), Hanyang University, Seoul 04763, Republic of Korea (e-mail: soyeon96@hanyang.ac.kr; awdrie21@hanyang.ac.kr; kkwandy@hanyang.ac.kr; myungseop@hanyang.ac.kr).

Jin-Cheol Park is with the Department of Automotive Engineering, Hanyang University, Seoul 04763, Republic of Korea, and also with the Samsung Electronics, Suwon 16677, Republic of Korea (e-mail: skensk1990@hanyang.ac.kr).

Jun-Woo Chin is with the Korea Automotive Technology Institute, Cheonan 31214, Republic of Korea (e-mail: jwchin@katech.re.kr).

Color versions of one or more figures in this article are available at https://doi.org/10.1109/TIA.2023.3314004.

Digital Object Identifier 10.1109/TIA.2023.3314004

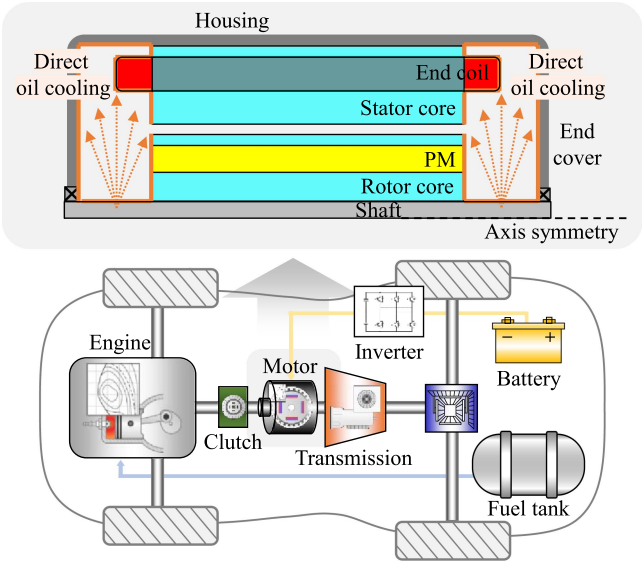

Fig. 1. Configuration of the P2 HEV.

Oil cooling directly cools the end windings; thus, the cooling efficiency is high, and the bearings can be lubricated [12]. An oil cooling system with high cooling efficiency is advantageous for the downsizing and high-power density of the motor. Because the electric motor of the parallel 2 (P2) HEV shown in Fig. 1 is located between the clutch and the transmission, a direct oil cooling system using automatic transmission fluid (ATF) can be applied to prevent the temperature of the motor from rising. Moreover, as the heat transfer through ATF is more complex and nonlinear than the electromagnetic behavior, it is difficult to quantify the HTC of the ATF [2], [13]. Additionally, the convection heat transfer by the ATF has different cooling characteristics depending on the inlet pressure, rotational speed, and position. Nevertheless, the oil cooling systems continue to be studied because they provide sufficient cooling when in direct contact with the generally hottest parts of the traction motor [12], [13], [14], [15], [16].

Thermal analysis methods for motors include lumped parameter thermal networks (LPTNs), finite element analysis (FEA), and computational fluid dynamics (CFD) [17], [18], [19]. Among these, LPTNs exhibit short analysis times; therefore, they have been effectively used to predict the temperature of various electric machines, including water-cooled surface-mounted PMSMs and PM spherical motors [20], [21]. An accurate evaluation of the HTC is required to improve the reliability of temperature prediction using LPTN. Similarly, thermal analysis through FEA increases the accuracy of the temperature estimation with logically defined boundary conditions and heat transfer methods. Boundary conditions such as the equivalent thermal conductivity of the air gap and natural convective resistance for the thermal analysis of a line-start PM motor in [22] are reflected based on empirical formulas. In [23], a thermal model based on the LPTN was calibrated using experimental data, and the test procedure was discussed for a systematic calibration process to be performed. The behavior of the sprayed oil investigated in [13] and [24] differed from that of the oil scattered through the shaft in this study. Therefore, the LPTN of the P2 HEV traction motor was modeled by changing and extending the thermal model and experimental procedures used in previous studies.

TABLE I
SPECIFICATIONS OF THE TRACTION MOTOR [1]

Motor Type	IPMSM	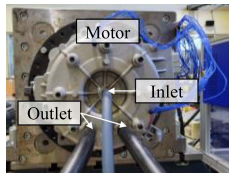 Traction motor
Number of poles/slots	16/24	
Stator / rotor outer diameter (Normalized)	1 / 0.714	
Active length (Normalized)	0.221	
Power (kW)	50	
Maximum speed (rpm)	6400	
Maximum current density (A_{rms}/mm^2)	14	
Cooling type	Oil cooling	Automatic transmission fluid
Oil temperature (°C)	60	
Oil flow rate (LPM)	1.2	

This study proposes a method of constructing an LPTN including direct oil cooling for a P2 HEV traction motor and performed a correlation process to estimate the heat dissipation by the ATF. In the correlation process, the experimentally measured and predicted temperatures are compared to determine the convective HTC of the ATF, and kriging surrogate model-based optimization is performed. The proposed direct oil cooling thermal model has high predictive accuracy and reflects the phenomenon caused by the direct oil cooling effect.

The remainder of this article is organized as follows: In Section II, the conductive heat resistance of the traction motor is calculated by applying the basic theory of LPTN, and the thermal model that reflects the direct oil cooling effect is proposed. The motor losses that are acting as heat sources are reflected in a direct oil-cooled LPTN developed via electromagnetic FEA and experiments. Section III describes the correlation process for determining the HTC of the ATF. The tests for temperature measurement were performed under various load conditions within a specific flow rate and driving range of the traction motor. The temperature prediction accuracy of the proposed direct oil-cooled LPTN is improved by performing the kriging surrogate model-based optimization. The predicted temperature with the LPTN under a different load condition is verified experimentally in Section IV. Finally, the conclusions of this study are presented in Section V.

II. THERMAL MODELING OF DIRECT OIL COOLED MOTOR

The specifications of the P2 HEV traction motor are presented in Table I. The geometric dimensions were normalized based on the outer diameter of the stator. The motor was cooled by ATF scattering from the rotating shaft. The ATF directly cools each part of the motor including the end winding and the PM, and is finally drained to the outlet. An LPTN is composed of a thermal resistor, thermal capacitor, and heat source. In an LPTN, heat

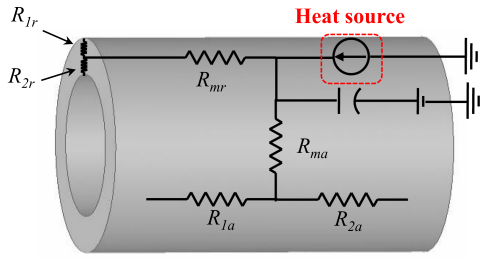

Fig. 2. Basic configuration of LPTN.

transfer is expressed as a thermal network based on the similarity between electrical and thermal systems. Thermal analysis via the LPTN has a short computation time; however, the accuracy of the temperature prediction depends on the boundary conditions that correspond to the HTCs. Three thermal models are developed and compared to effectively reflect the heat dissipation due to direct oil cooling.

A. Conduction, Contact and Convection Heat Transfer

In the LPTN, the shape of each part can be assumed to be equivalent to that of a hollow cylinder because the motor is a rotating device, as depicted in Fig. 2. The conductive thermal resistance was modeled as a network composed of axial and radial thermal resistances. In Fig. 2, R_{1r}, R_{2r}, and R_{mr} represent the thermal resistances in the radial direction; R_{1a}, R_{2a}, and R_{ma} represent the thermal resistances in the axial direction; Q represents the heat source; and C represents the thermal capacitance. Unlike FEA, the LPTN cannot analyze the temperature distribution of each element within each part. Since LPTN equalizes each part of a motor composed of numerous elements into one lumped parameter, it provides the maximum temperature in the absence of compensated thermal resistance; therefore, negative conduction thermal resistances are required in the radial and axial directions to prevent overestimation of the temperature for each part [25]. To predict the average temperature, the negative conduction thermal resistance compensates for the temperature so that the temperature increase owing to the overlap of internal heat generation is not reflected. Assuming that the radial and axial heat transfers are independent, and that the axial temperature of the hollow cylinder is parabolic, the one-dimensional axial conduction heat transfer equation in the steady state is expressed as

$$\frac{\partial}{\partial x}\left(k\frac{\partial T}{\partial x}\right)+\dot{g}=0 \tag{1}$$

where x denotes the length; k stands for the thermal conductivity; T denotes the temperature, and $\dot{g}$ indicates the heat generation per unit volume. Similarly, the radial conduction heat transfer equation in steady state is as follows:

$$\frac{\partial^2 T}{\partial r^2}+\frac{1}{r}\frac{\partial T}{\partial r}+\frac{\dot{g}}{k}=0 \tag{2}$$

where r denotes the radius. The thermal resistance was calculated as the ratio of the difference in temperature to heat generation. Therefore, using (1) and (2), the conduction thermal resistance in each direction was calculated from the dimensions and material properties, which are expressed in (3)–(7).

$$R_{r1}=\frac{1}{2\pi k_r L}\left[1-\frac{2r_1^2\ln\left(r_2/r_1\right)}{\left(r_2^2-r_1^2\right)}\right] \tag{3}$$

$$R_{r2}=\frac{1}{2\pi k_r L}\left[\frac{2r_2^2\ln\left(r_2/r_1\right)}{\left(r_2^2-r_1^2\right)}-1\right] \tag{4}$$

$$R_{r3}=\frac{-1}{4\pi(r_2^2-r_1^2)k_r L}\left[r_1^2+r_2^2-\frac{4r_2^2r_1^2\ln\left(r_2/r_1\right)}{\left(r_2^2-r_1^2\right)}\right] \tag{5}$$

$$R_{a1},R_{a2}=\frac{L}{2\pi k_a(r_2^2-r_1^2)} \tag{6}$$

$$R_{a3}=\frac{-L}{6\pi k_a(r_2^2-r_1^2)} \tag{7}$$

where k_a and k_r denote the axial and radial thermal conductivities, respectively. The impregnated winding reflects the radial equivalent thermal conductivity, not the thermal conductivity of copper. Considering the thermal properties of the conductor and electrical insulation, the radial equivalent thermal conductivity of the impregnated winding was 2−10 W/m °C [26]. Moreover, the circumferential conduction heat transfer between the stator teeth and windings was considered. The circumferential thermal resistance reflecting the parallel-connected teeth was calculated as follows:

$$R_{teeth\_c}=\frac{\pi\phi_e r_m}{k_t L_s s\phi_p\left(r_{t\_\text{out}}-r_{t\_\text{in}}\right)n^2} \tag{8}$$

where ϕ_e symbolizes the equivalent length of the tooth; r_m denotes the logarithmic mean radius of the teeth; k_t indicates the thermal conductivity of the teeth; L_s denotes the stack length; s indicates the stacking factor; ϕ_p indicates the pitch of the tooth; r_{t_out} denotes the outer radius of the teeth; r_{t_in} denotes the inner radius of the teeth, and n is the number of slots. The thermal capacitance of each part of the motor is expressed as follows:

$$C=c_p\rho\pi L\left(r_2^2-r_1^2\right). \tag{9}$$

where c_p indicates the specific heat and ρ refers to the material density. The thermal capacitance allows the transient state to be considered in thermal analysis using the LPTN.

The contact thermal resistances between the housing and stator yoke, PM and rotor core, and rotor core and shaft are calculated as (10)

$$R_{cont}=\frac{1}{h_{cont}A} \tag{10}$$

where h_{cont} denotes the boundary film coefficient of the contact heat transfer, and A denotes the surface area in contact. The contact HTC depends on the contact pressure and manufacturing process and is in the range of 2000−10000 W/m^2 °C [10]. The HTC on convective surfaces can be calculated based on proven empirical formulas for natural and forced convection [11]. The convection heat transfer between the housing and the ambient environment was modeled using natural convective thermal resistance. The natural convective HTC was 5−55 W/m^2 °C [22], [27]. In addition, convective heat is transferred between the air gap and stator teeth/rotor core, and between the end cap

TABLE II
PARAMETERS FOR LOSSES ANALYSIS

Parameter		*Value*	*Unit*
PM	Residual induction	1.243	T
	Recoil permeability	1.05	-
	Resistivity	1.4	μΩm
Core	Density	7600	kg/m^3
	Thickness	0.25	mm
Armature	Phase resistance	0.016	Ω
	Maximum current	228	A_{rms}

air and each component. The convective thermal resistance was also calculated as (11)

$$R_{conv} = \frac{1}{h_{conv} A} \tag{11}$$

where h_{conv} represents convective HTC. The convective HTC of the air gap is calculated as (12)

$$h_{gap} = k_d \frac{Nu}{l_{gap}} \tag{12}$$

where k_d denotes the fluid conductivity, *Nu* is the Nusselt number, and l_{gap} denotes the air gap length. The convective HTC of the air gap is a function of the speed, fluid kinematic viscosity, Prandtl number, density, and specific heat [28].

B. Heat Source

Traction motor losses include copper, iron, PM eddy current, and mechanical losses. The motor losses act as heat sources. Electromagnetic losses were calculated using FEA, and the analysis conditions are listed in Table II [1]. The armature phase resistance was measured to calculate the copper loss. Iron loss occurs in the stator core and rotor core, and it includes hysteresis and eddy current losses. Although the rotor iron loss is smaller than that of the stator, the magnetic flux density changes with time due to the slotting effect and magnetic saturation, resulting in rotor iron loss. A transient electromagnetic analysis was performed to consider the nonlinearity of the core material using 2-dimensional (2D) FEA. In the iron loss calculation process, the harmonics were analyzed for the magnetic flux density of one electrical period, calculated using 2D FEA performed on one element. Based on the measured iron loss data, the iron loss of one element was determined by considering the operating frequency and harmonic order. The process was repeated for all elements, and the sum of the iron losses for each element was calculated as the total iron loss of the motor. The stator of LPTN was composed of separate parts in which the yoke, teeth, and tooth tip each have their own nodes. In addition, the rotor was also separated into an outer rotor and an inner rotor; therefore, the calculated total iron loss was divided into each part and reflected as a heat source. The PM eddy current loss refers to the power loss caused by the resistance of the conductor to the eddy current generated by the time-varying magnetic field. Because the PM is a conductor, the eddy currents are generated, and PM

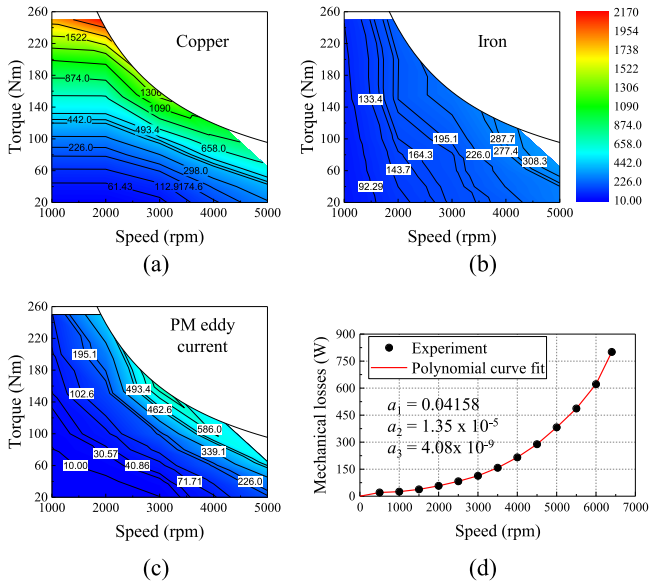

Fig. 3. Heat source: (a) copper loss, (b) iron loss, (c) PM eddy current loss, and (d) mechanical loss.

eddy current loss was reflected as a heat source at the PM node in LPTN by performing 3-dimensional (3D) FEA to consider the z-axis path of the eddy current. The calculated electromagnetic losses are shown in Fig. 3(a)–(c). As the iron loss may occur owing to magnetized PM, the mechanical losses are reflected through no-load tests on unmagnetized PMs performed at 60 °C. The mechanical losses consist of the bearing and windage losses, expressed as follows:

$$P_{mech} = P_{bearing} + P_{windage} = a_1\omega + a_2\omega^2 + a_3\omega^3, \tag{13}$$

where ω denotes the speed, and a_1, a_2, and a_3 are coefficients. To estimate the coefficients, polynomial curve fitting was performed based on the no-load test data shown in Fig. 3(d). The sum of the linear and quadratic terms represents the bearing loss, and the windage loss is proportional to the cubic speed. As a_3 is smaller than a_1 and a_2, the bearing loss dominates the mechanical losses. Therefore, the mechanical loss is reflected as a heat source at the end cover.

C. Heat Dissipation by Automatic Transmission Fluid

Appropriate heat dissipation modeling is important to develop direct oil-cooled LPTNs with the cooling effect of ATF, which has a complex and nonlinear behavior. As shown in Fig. 4, three methods were reviewed to effectively reflect heat dissipation by ATF. Heat dissipation was modeled as a heat sink in LPTN, and the final model that reflected the direct oil cooling effect was determined through a comparison between the developed models. The ATF is scattered inside the motor by the rotation of the motor shaft and cannot be completely drained due to its viscosity. Therefore, the cooling effect by ATF acts on each part of the motor. The part that reflects oil cooling through heat sink modeling can be end-cap air, or it can be a node for each part affected by the cooling oil. In addition, the amount

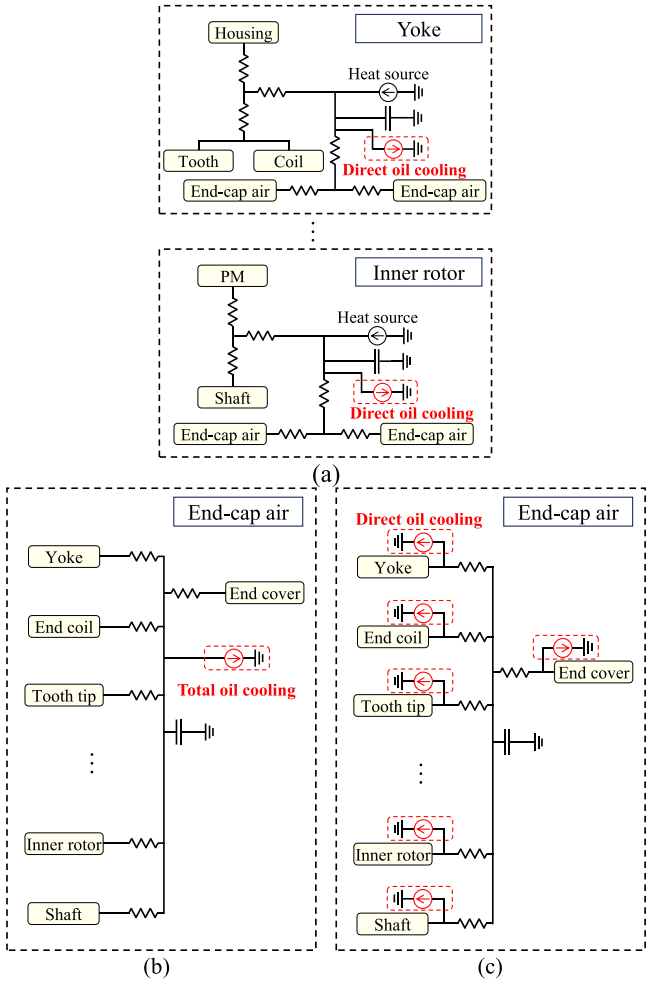

Fig. 4. Heat sink modeling: (a) method 1; single current source at node of each component, (b) method 2; single current source at end-cap air, and (c) method 3; multiple current sources at end-cap air.

of heat dissipation can be calculated by considering the total heat dissipation from the average temperature of each part or by estimating the heat dissipation of each part from the temperature of each component. The total heat dissipation is calculated as:

$$Q_{\mathrm{ATF}} = h_{\mathrm{ATF}} A \left(T_{\mathrm{average}} - T_{\mathrm{ATF}}\right) \tag{14}$$

where h_{ATF} indicates the convective HTC of the ATF, T_{average} indicates the average temperature of each part affected by the ATF, and T_{ATF} denotes the temperature of the ATF. The heat dissipation from the temperature of each component by ATF is calculated as follows:

$$Q_{\mathrm{ATF}} = h_{\mathrm{ATF}} A \left(T_{\mathrm{component}} - T_{\mathrm{ATF}}\right) \tag{15}$$

where $T_{\mathrm{component}}$ denotes the temperature of a specific component of the motor in contact with the ATF. The heat dissipation in Fig. 4(a) and (c) is calculated as (15), and the heat dissipation in Fig. 4(b) is calculated as (14).

In method 1 of Fig. 4(a), heat sink was modeled at the nodes of each part affected by cooling by ATF. With method 1, the oil cooling effect for each part can be reflected independently, but the heat source and heat dissipation act simultaneously on the same node. Therefore, there is a problem in that the cooling effect is overestimated when the heat dissipation is greater than that of the heat source due to the arbitrary convective HTC by the ATF. The minimum temperature inside the motor is limited to 60 °C owing to the ATF supplied from the transmission, whereas the thermal model of method 1 may predict a motor temperature below 60 °C due to the excessive cooling effect. In the thermal models of methods 2 and 3, the cooling effect by the ATF is applied in the end-cap air. The total heat dissipation calculated from the average temperature of the motor is applied to the heat dissipation modeling through method 2 in Fig. 4(b). Since the only unknown parameter is the convective HTC by the ATF, the computational time required for the correlation process performed to estimate the total heat dissipation by the ATF can be reduced. The higher the frequency, the greater the iron loss and PM eddy current loss, which increases the rotor temperature, but oil scattering through the rotating motor shaft cools the protruding end winding more effectively. However, modeling with method 2 does not reflect the phenomenon that the rotor temperature is higher than the end winding temperature under high-speed load conditions. Besides, the average temperature of the motor for calculating the total heat dissipation is also an uncertain parameter. The ATF acts to prevent the temperature rise of the motor in the end-cap air, so the main heat transfer path is formed in the end-cap air. In addition, the cooling effect of the ATF is different for each part of the motor. Therefore, the effective method to model the cooling effect by the ATF behavior is Fig. 4(c).

Fig. 5 shows the developed direct oil-cooled LPTN including heat sources, thermal resistances, thermal capacitances, and heat dissipation modeling of method 3. The developed direct oil-cooled LPTN was used to predict the temperature according to the HTC of the ATF in the correlation process. The convective HTC of the ATF was optimized through correlation with the temperature measurement experiment. In the proposed thermal model, the equivalent thermal conductivity, contact heat transfer coefficient, and natural convective heat transfer coefficient, which are relatively independent of the load conditions compared to the convective heat transfer coefficient of oil cooling, were reflected as 2 W/m °C, 2000 W/m^2 °C, and 5 W/m^2 °C, respectively.

III. Proposed Correlation Process

The kriging surrogate model-based optimization of convective HTCs by ATF was performed to improve the reliability of the oil-cooled thermal model. HTCs of the ATF were determined through correlation with experiments. The proposed correlation process is illustrated in Fig. 6. Cooling by the ATF works differently for each part of the motor, and convective heat transfer by the ATF depends on the cooling effect of the ATF. Therefore, the HTC of the ATF for each component was determined as a variable. A design of experiment (DOE) was performed for the variables. Using the configured direct oil-cooled LPTN, the motor temperature was predicted according to the sample points extracted by the DOE. The predicted temperature is compared with the experimentally measured temperature to calculate the

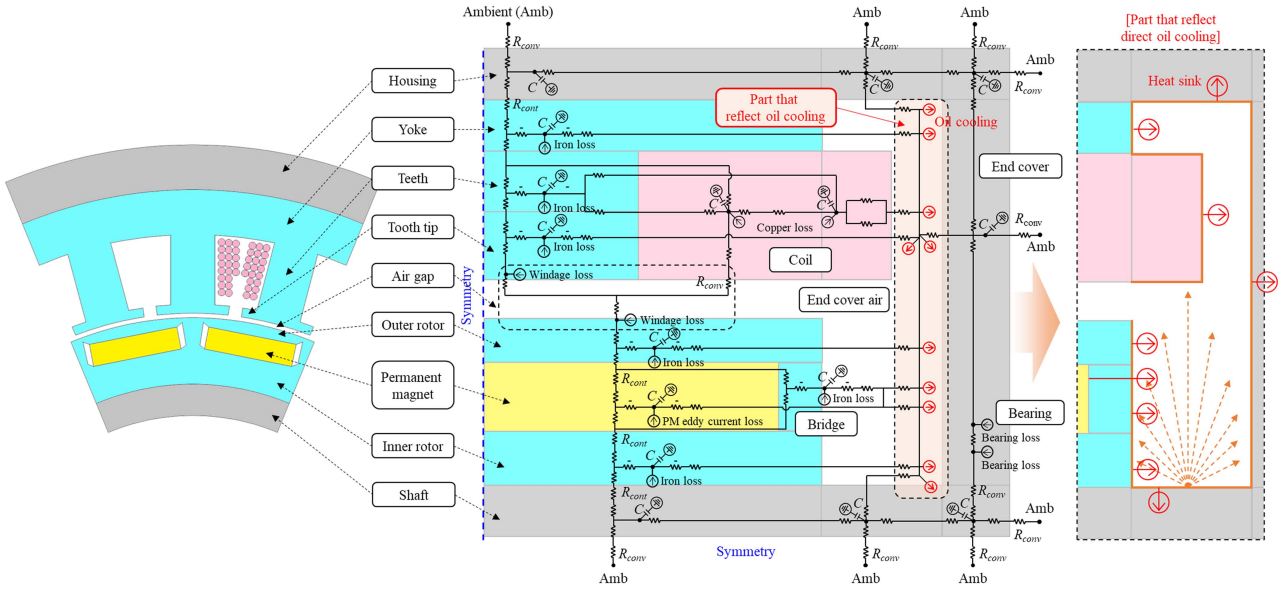

Fig. 5. Direct oil cooled LPTN developed through method 3.

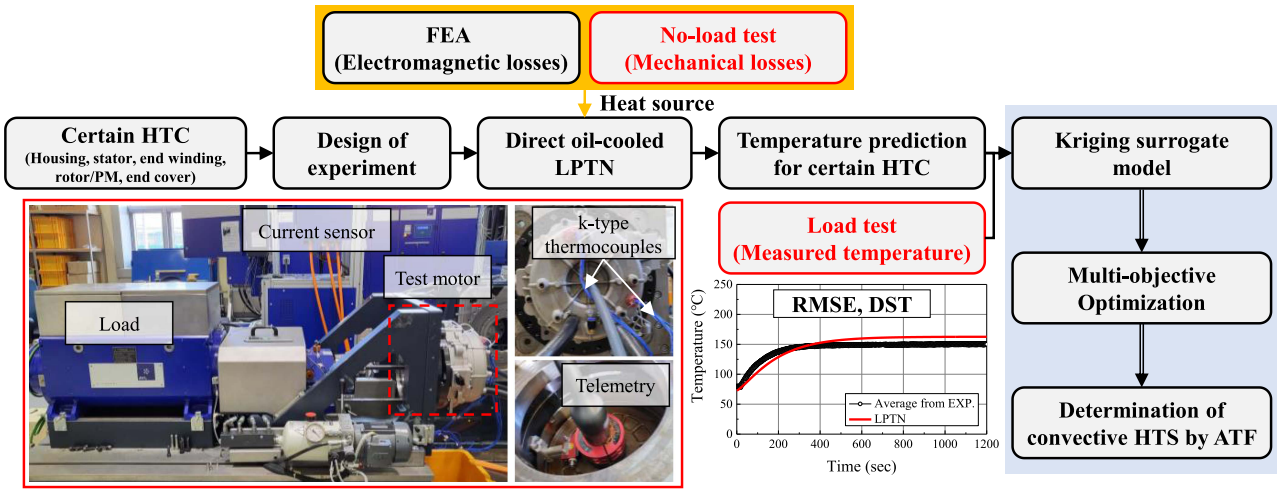

Fig. 6. Proposed correlation process.

root-mean-square error (RMSE) of the two temperatures and the difference between the two saturation temperatures (DST). The saturation temperature was not measured to prevent damage to the motor under high-load conditions, which are subject to derating control. Therefore, the temperature difference at the end point of the transient region, rather than the DST, was calculated under the high-load condition. To generate the kriging surrogate model, the variables corresponding to the HTCs of the ATF and the calculated RMSE and DST were reflected in the design variables and responses, respectively. Optimization was performed based on the generated kriging surrogate model, and the HTCs of the ATF were determined under specific load conditions.

A. *Load Test for Temperature Measurement*

A load test was conducted to measure the temperature of the traction motor, as presented in Fig. 6. The ATF temperature was 60 °C when considering the transmission, and the flow rate was constantly controlled at 1.2 LPM using an oil chiller. As the control performance deteriorates, the ATF fills the inside of the traction motor, and the mechanical loss owing to the viscosity of the ATF increases; therefore, it is crucial to control the flow rate of the ATF. The stator temperatures corresponding to the stator yoke, stator winding, and end winding were measured using k-type thermocouples and the rotor temperature was measured using telemetry. As k-type thermocouple was used to measure the stator temperature, the hole drilled in the end cover was sealed for ATF control. The telemetry system, which consists of an antenna and a receiver, transmits the rotor temperature as a voltage level to the data acquisition system via a Bayonet Neill Concelman connector. The load speed and motor torque were controlled. Convective HTCs by direct cooling with liquids are given over a wide range [17]. In order to accurately estimate convective HTCs of ATF according to load conditions, the tests were performed at 30 operating points, as specified in Table III. A

TABLE III
OPERATING POINTS TO LOAD TEST

Torque (Nm)	250	250	-	-	-
	200	200	-	-	-
	150	150	160	-	-
	100	100	100	100	-
	80	80	80	80	-
	60	60	60	60	65
	40	40	40	40	40
	20	20	20	20	20
Speed (rpm)	1000	2000	3000	4000	5000
Efficiency map	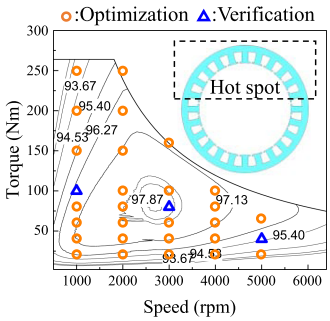				

temperature saturation test of the traction motor was performed for more than 60 min within the continuous rating. The test was conducted until the winding temperature reached 180 °C under certain high-load conditions, excluding continuous ratings. The 30 operating points indicated in the efficiency map of Table III are classified as follows.

- 27 operating points corresponding to orange circles; These were the sample points on which optimization was performed.
- 3 operating points corresponding to blue triangles; It was used to validate the developed direct oil-cooled LPTN, without any optimization performed.

Fig. 7 shows the temperature measured at the weak cooling point under specific load conditions. In particular, the stator temperature depends on the location where the k-type thermocouple is attached, owing to the influence of gravity on the ATF. The end winding temperature indicated in Fig. 7(b) is the temperature of the winding that protrudes into the end-cap air, and the stator winding temperature indicated in Fig. 7(c) is the winding temperature of the active part in contact with the stator teeth. The end winding temperatures are lower than the stator winding temperatures. This phenomenon can be explained by the cooling effect of the direct oil cooling system. Structurally, it is difficult to cool the stator winding through direct contact with the ATF; however, it is indirectly affected by the cooling effect of the end winding.

B. Optimization Variables

The convective HTC of the ATF is different in the housing, stator, end winding, rotor, and end cover. The ranges of the variables were determined by considering the temperature

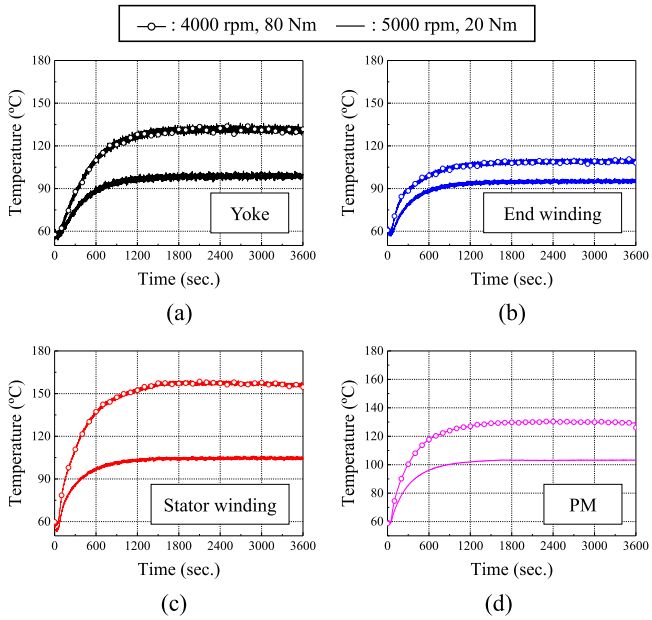

Fig. 7. Measured temperature: (a) yoke temperature, (b) end winding temperature, (c) stator winding temperature, and (d) PM temperature.

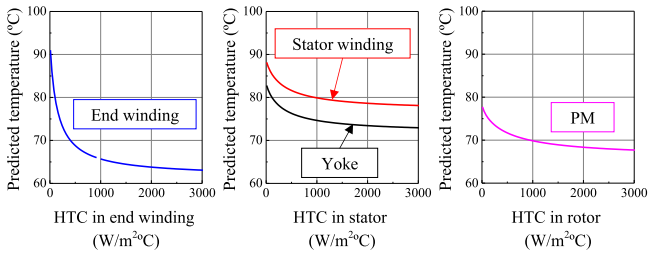

Fig. 8. Predicted temperature according to the convective HTC by the ATF: (a) end winding, (b) stator winding and yoke, and (c) PM.

change in each part using the configured LPTN. As shown in Fig. 8, the temperature predicted by the ATF according to the convective HTC is nonlinear; the heat source is reflected when the motor speed is 1000 rpm and the motor torque is 80 Nm. The convective HTC obtained by the ATF is used to calculate the heat dissipation in (15). To develop a kriging model, a DOE, in which 900 sample points were extracted for variables, was performed.

C. Kriging Surrogate Model

A surrogate model presents a functional relationship between a variable and a response, with a short computational time and good accuracy [29]. The kriging surrogate model is a type of surrogate model used to predict nonlinear responses [30], [31]. As cooling by an ATF is a complex and nonlinear problem, the kriging surrogate model can provide a useful solution. This model is generated by modeling the Gaussian process and used for optimization in the correlation process to determine the convective HTCs of the ATF corresponding to the variables in which the predicted temperature using the

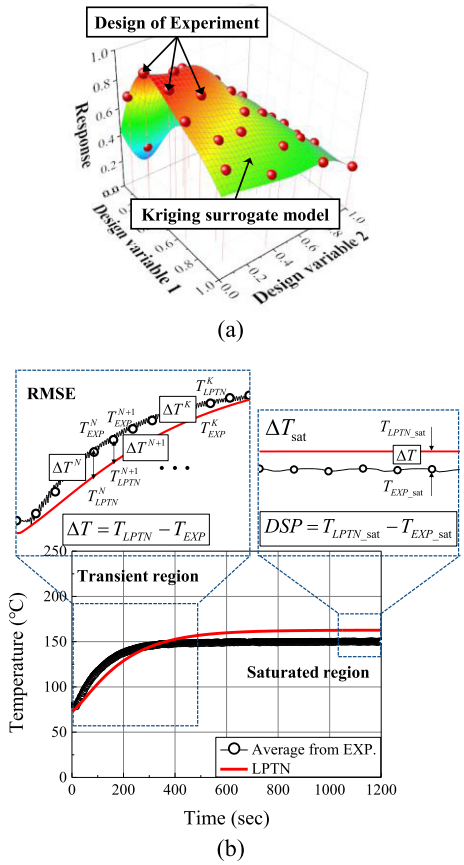

Fig. 9. (a) Kriging surrogate model. (b) Objective function.

LPTN matches the experimentally measured temperature. The RMSE and the DST values corresponding to the responses in Fig. 9(a) were calculated using (16) and (17) [1], respectively, in Fig. 9(b).

$$\text{RMSE} = \sqrt{\frac{1}{n}\sum_{i=1}^{n}\left(T_{LPTN} - T_{EXP}\right)^2} \tag{16}$$

$$\text{DST} = T_{LPTN\_\text{sat}} - T_{EXP\_\text{sat}} \tag{17}$$

where n is the number of measured temperature data points in the transient region, T_{LPTN} indicates the predicted temperature using the direct oil-cooled LPTN, T_{EXP} represents the experimentally measured temperature, T_{LPTN_sat} denotes the predicted saturation temperature, and T_{EXP_sat} indicates the measured saturation temperature.

D. Optimization

The multi objective function of the kriging surrogate model-based optimization minimizes the difference between the predicted and measured temperatures. The optimization method was selected so that sequential quadratic programming (SQP) could provide a solution to the nonlinear problem. As shown in Fig. 10 [1], the SQP method iteratively evaluates the gradient of the objective function with respect to the parameters used to solve nonlinear problems. For complex nonlinear problems, the

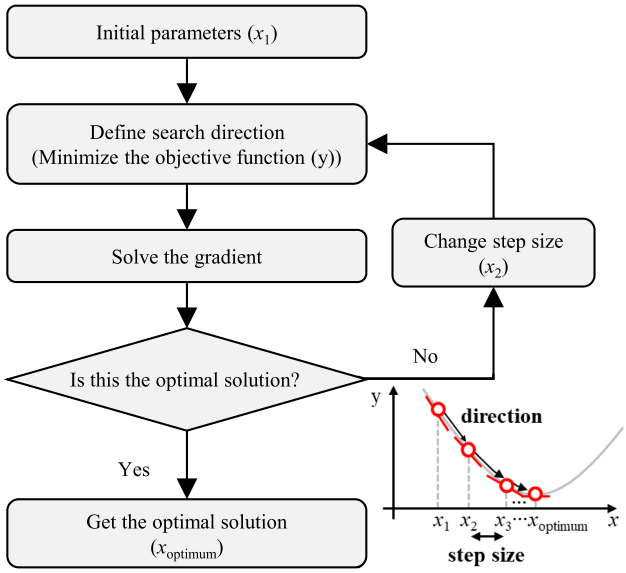

Fig. 10. Sequential quadratic programming.

optimal solution may depend on the parameters. As the optimal solution of a complex nonlinear problem may vary depending on the initial parameters, optimal solutions according to 100 initial parameters were derived to determine the convective HTCs of the ATF. The optimal HTCs of the ATF shown in Fig. 11 were determined under 27 load conditions. The optimal HTCs of the ATF tended to increase with the motor speed and torque. Fig. 12 shows that the optimization within the correlation process to determine convective HTCs by the ATF of direct oil-cooled LPTN was performed successfully. As the RMSEs for each component are less than 10%, and DSTs are less than 10 °C. At the predicted temperature shown in Fig. 12, the end winding temperatures were lower than the stator winding temperatures. Therefore, the constructed thermal model reflected the phenomena caused by the direct oil cooling effect. In addition to the 27 load conditions for optimization, the measured temperatures at the three shaded load conditions indicated in Table III were used to verify that developed direct oil-cooled LPTN reflects the optimal HTCs of the ATF.

IV. Experimental Verification

To verify the validity of the developed direct oil-cooled LPTN, the temperatures estimated using the configurated LPTN were compared with the test results under three load conditions (see the shaded load conditions given in Table III), as shown in Fig. 13. For verification of the developed thermal model, optimization was not performed for the three operating points. The heat source to estimate the temperature is listed in Table IV, and the flow rate of ATF is 1.2 LPM. In Fig. 13, the maximum values of RMSE and DSP are 6.6% and 4.8 °C, respectively. The direct oil-cooled thermal model has high prediction accuracy. Moreover, the temperature predicted by the LPTN shows a tendency similar to that of the actual temperature of each

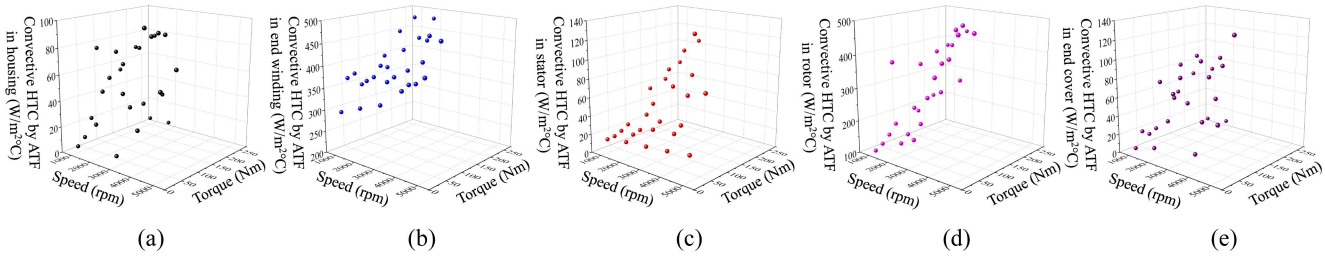

Fig. 11. Optimal HTCs by ATF: (a) housing, (b) end winding, (c) stator, (d) rotor, and (e) end cover.

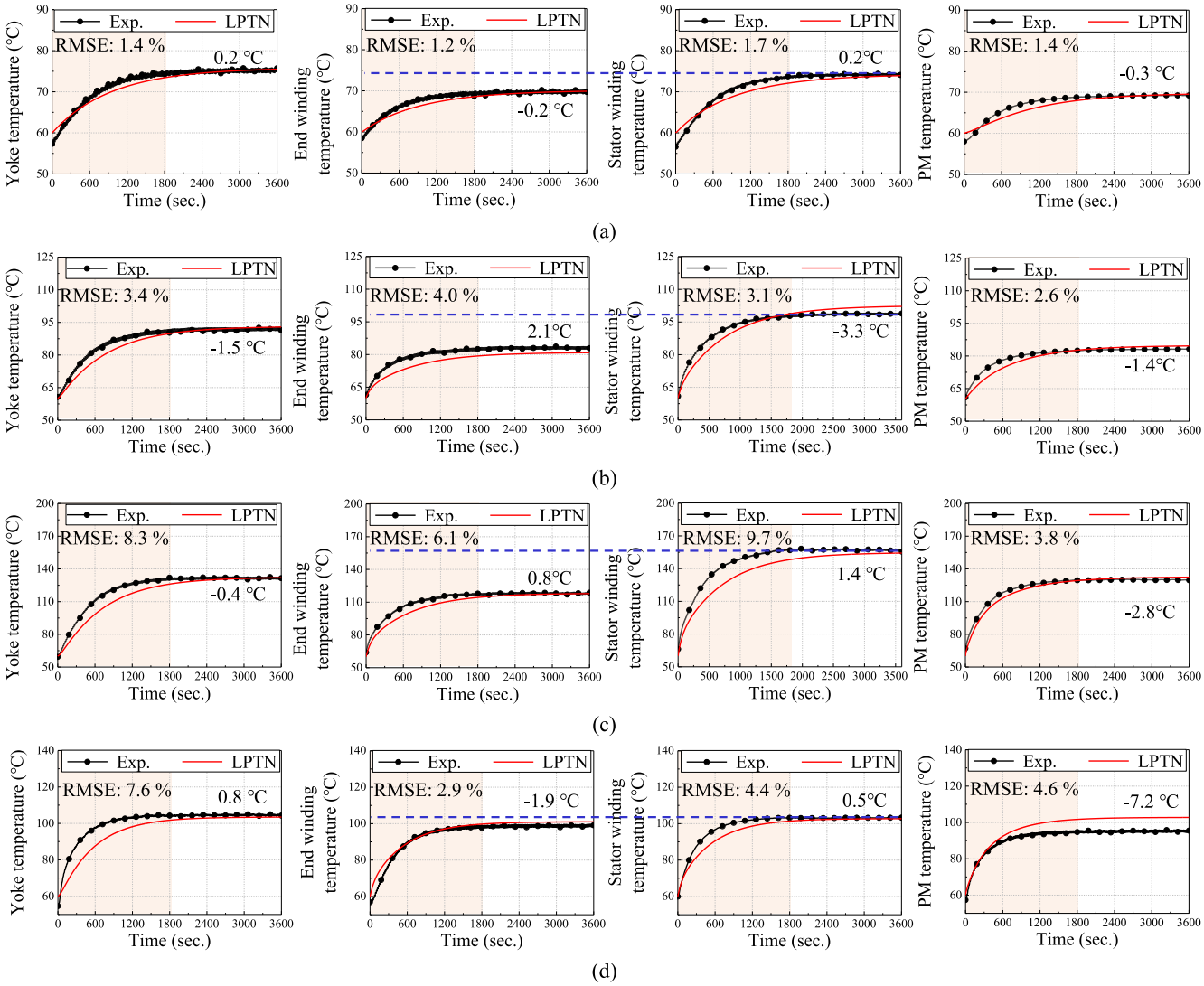

Fig. 12. Results of comparing the measured and predicted temperatures at sample points: (a) 2000 rpm and 20 Nm, (b) 3000 rpm and 100 Nm, (c) 4000 rpm and 80 Nm, and (d) 5000 rpm and 20 Nm.

component. As the speed increases, the cooling effect of the ATF also increases, but the PM eddy current loss also increases; therefore, the PM temperature is high at 5000 rpm and 40 Nm. Although the cooling effect decreases, the component temperatures were low because the heat source is relatively small at 1000 rpm and 100 Nm. These results show that the proposed correlation process is useful for determining convective HTCs of the ATF. In addition, the accuracy of temperature prediction of the traction motor for the P2 HEV has been improved through the developed direct-oil cooled LPTN.

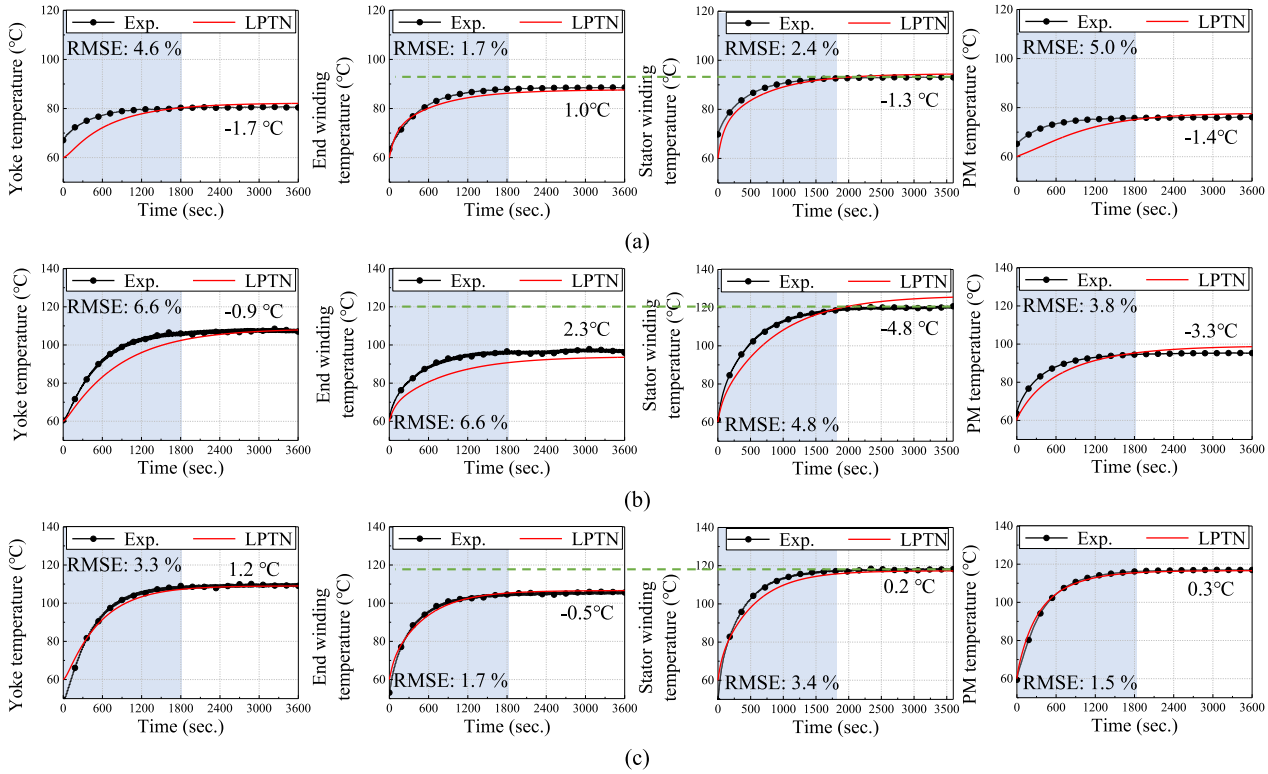

Fig. 13. Results of comparing the measured and predicted temperatures at verification points: (a) 1000 rpm and 100 Nm, (b) 3000 rpm and 80 Nm, and (c) 5000 rpm and 40 Nm.

TABLE IV
HEAT SOURCE

Load condition	Speed (rpm)	1000	3000	5000
	Torque (Nm)	100	80	40
Copper loss (W)		276.9	295.5	384.2
Iron loss (W)		62.6	182.9	276.6
PM eddy current loss (W)		15.2	115.0	282.0
Bearing loss (W)		25.1	113.1	382.2

V. CONCLUSION

A direct oil-cooled LPTN of the P2 HEV traction motor was developed, reflecting the convective HTCs of the ATF determined under 27 load conditions. In this study, a correlation process for convective HTCs of ATF was proposed, and kriging surrogate model-based optimization was performed to determine the convective HTCs of the ATF. Therefore, the direct oil-cooled LPTN with convective HTCs of the ATF, determined using the same correlation process under various load conditions, can estimate the temperature with high accuracy over the driving range of the traction motor. The configured direct oil-cooled LPTN can be utilized to identify the temperature trend based on the shape of the motor and flow rate. Furthermore, the tendency analysis of HTCs according to load conditions is conducive to predicting the behavior of ATF in terms of thermal management.

REFERENCES

[1] S.-Y. Im, T.-G. Lee, K.-W. Kim, J.-C. Park, J.-W. Chin, and M.-S. Lim, "Thermal modeling with surrogate model-based optimization of direct oil cooling heat transfer coefficient for HEV motor," in *Proc. IEEE Energy Convers. Congr. Expo.*, 2022, pp. 1–7, doi: 10.1109/ECCE50734.2022.9947410.

[2] K. Bennion and G. Moreno, "Convective heat transfer coefficients of automatic transmission fluid jets with implications for electric machine thermal management," in *Proc. Int. Tech. Conf. Exhib. Packag. Integration Electron. Photon. Microsystems Int. Conf. Nanochannels, Microchannels, Minichannels*, 2015, Art. no. V003T04A010.

[3] J. Fan et al., "Thermal analysis of permanent magnet motor for the electric vehicle application considering driving duty cycle," *IEEE Trans. Magn.*, vol. 46, no. 6, pp. 2493–2496, Jun. 2010.

[4] F. JinXin, Z. ChengNing, W. ZhiFu, and E. G. Strangas, "Thermal analysis of water cooled surface mount permanent magnet electric motor for electric vehicle," in *Proc. IEEE Int. Conf. Elect. Mach. Syst.*, 2010, pp. 1024–1028.

[5] P.-O. Gronwald and T. A. Kern, "Traction motor cooling systems, a literature review and comparative study," *IEEE Trans. Transp. Electrific.*, vol. 7, no. 4, pp. 2892–2913, Dec. 2021.

[6] A. Tuysuz, F. Meyer, M. Steichen, C. Zwyssig, and J. W. Kolar, "Advanced cooling methods for high-speed electrical machines," *IEEE Trans. Ind. Appl.*, vol. 53, no. 3, pp. 2077–2087, May/Jun. 2017.

[7] J. Huang et al., "A hybrid electric vehicle motor cooling system – design, model, and control," *IEEE Trans. Veh. Technol.*, vol. 68, no. 5, pp. 4465–4478, May 2019.

[8] P. Liang, F. Chai, K. Shen, and W. Liu, "Water jacket and slot optimization of a water-cooling permanent magnet synchronous in-wheel motor," *IEEE Trans. Ind. Appl.*, vol. 57, no. 3, pp. 2431–2439, May/Jun. 2021.

[9] X. Yang, A. Fatemi, T. Nehl, L. Hao, W. Zeng, and S. Parrish, "Comparative study of three stator cooling jackets for electric machine of mild hybrid vehicle," *IEEE Trans. Ind. Appl.*, vol. 57, no. 2, pp. 1193–1201, Mar./Apr. 2021.

[10] D. P. Kulkarni, G. Rupertus, and E. Chen, "Experimental investigation of contact resistance for water cooled jacket for electric motors and generators," *IEEE Trans. Energy. Convers.*, vol. 27, no. 1, pp. 204–210, Mar. 2012.

[11] B. Guo, Y. Huang, Y. Guo, and J. Zhu, "Thermal analysis of the conical rotor motor using LPTN with accurate heat transfer coefficients," *IEEE Trans. Appl. Supercond.*, vol. 26, no. 7, Oct. 2016, Art. no. 0611507.
[12] M. H. Park and S. C. Kim, "Thermal characteristics and effects of oil spray cooling on in-wheel motors in electric vehicles," *Appl. Thermal Eng.*, vol. 152, pp. 582–593, Apr. 2019.
[13] F. Zhang et al., "A thermal modeling approach and experimental validation for an oil spray-cooled hairpin winding machine," *IEEE Trans. Transp. Electrific.*, vol. 7, no. 4, pp. 2914–2926, Dec. 2021.
[14] Y. Gai, Y. C. Chong, H. Adam, X. Deng, M. Popescu, and J. Goss, "Thermal analysis of an oil-cooled shaft for a 30 000 r/min automotive traction motor," *IEEE Trans. Ind. Appl.*, vol. 56, no. 6, pp. 6053–6061, Nov./Dec. 2020.
[15] C. Liu et al., "Experimental investigation on oil spray cooling with hairpin windings," *IEEE Trans. Ind. Electron.*, vol. 67, no. 9, pp. 7343–7353, Sep. 2020.
[16] A. J. Bourgault, P. Roy, E. Ghosh, and N. C. Kar, "A survey of different cooling methods for traction motor application," in *Proc. IEEE Can. Conf. Elect. Comput. Eng.*, 2019, pp. 1–4.
[17] Y. Gai et al., "Cooling of automotive traction motors: Schemes, examples, and computation methods," *IEEE Trans. Ind. Electron.*, vol. 66, no. 3, pp. 1681–1692, Mar. 2019.
[18] R. A. Torres, H. Dai, W. Lee, T. M. Jahns, and B. Sarlioglu, "Cooling design of integrated motor drives using analytical thermal model, finite element analysis, and computational fluid dynamics," in *Proc. Appl. Power Electron. Conf., Virtual Conf.*, 2021, pp. 1509–1509.
[19] F. Ahmed, P. Roy, M. Towhidi, G. Feng, and N. C. Kar, "CFD and LPTN hybrid technique to determine convection coefficient in end-winding of TEFC induction motor with copper rotor," in *Proc. 45th Annu. Conf. IEEE Ind. Electron. Soc.*, 2019, pp. 939–944.
[20] J. X. Fan, C. N. Zhang, Z. Wang, and E. G. Strangas, "Thermal analysis of water cooled surface mount permanent magnet electric motor for electric vehicle," in *Proc. Int. Conf. Elect. Mach. Syst.*, 2010, pp. 1024–1028.
[21] H. Li and Y. Shen, "Thermal analysis of the permanent-magnet spherical motor," *IEEE Trans. Energy Convers.*, vol. 30, no. 3, pp. 991–998, Sep. 2015.
[22] M. F. Palangar, A. Mahmoudi, S. Kahourzade, and W. L. Soong, "Electromagnetic and thermal analysis of a line-start permanent-magnet synchronous motor," in *Proc. IEEE Energy Convers. Congr. Expo.*, 2020, pp. 502–508.
[23] A. Boglietti, M. Cossale, M. Popescu, and D. A. Staton, "Electrical machines thermal model: Advanced calibration techniques," *IEEE Trans. Ind. Appl.*, vol. 55, no. 3, pp. 2620–2628, May/Jun. 2019.
[24] C. Liu et al., "Estimation of oil spray cooling heat transfer coefficients on hairpin windings with reduced-parameter models," *IEEE Trans. Transp. Electrific.*, vol. 7, no. 2, pp. 793–803, Jun. 2021.
[25] B.-K. Song, J.-W. Chin, D.-M. Kim, K.-Y. Hwang, and M.-S. Lim, "Temperature estimation using lumped-parameter thermal network with piecewise stator-housing modules for fault-tolerant brake systems in highly automated driving vehicles," *IEEE Trans. Intell. Transp. Syst.*, vol. 22, no. 9, pp. 5819–5832, Sep. 2021.
[26] N. Simpson, R. Wrobel, and P. H. Mellor, "Estimation of equivalent thermal parameters of impregnated electrical windings," *IEEE Trans. Ind. Appl.*, vol. 49, no. 6, pp. 2505–2515, Nov./Dec. 2013.
[27] D. G. Dorrell, M.-F. Hsieh, M. Popescu, L. Evans, D. A. Staton, and V. Grout, "A review of the design issues and techniques for radial-flux brushless surface and internal rare-earth permanent-magnet motors," *IEEE Trans. Ind. Electron.*, vol. 58, no. 9, pp. 3741–3757, Sep. 2011.
[28] D. A. Howey, P. R. N. Childs, and A. S. Holmes, "Air-gap convection in rotating electrical machines," *IEEE Trans. Ind. Electron.*, vol. 59, no. 3, pp. 1367–1375, Mar. 2012.
[29] S.-Y. Im, S.-G. Lee, D.-M. Kim, G. Xu, S.-Y. Shin, and M.-S. Lim, "Kriging surrogate model-based design of an ultra-high-speed surfaced-mounted permanent-magnet synchronous motor considering stator iron loss and rotor eddy current loss," *IEEE Trans. Magn.*, vol. 58, no. 2, Feb. 2022, Art. no. 8101405.
[30] S. Kim, S.-G. Lee, J.-M. Kim, T. H. Lee, and M.-S. Lim, "Robust design optimization of surface-mounted permanent magnet synchronous motor using uncertainty characterization by bootstrap method," *IEEE Trans. Energy Convers.*, vol. 35, no. 4, pp. 2056–2065, Dec. 2020.
[31] L. Lebensztajn, C. A. RondiniMarretto, M. Caldoracosta, and J.-L. Coulomb, "Kriging: A useful tool for electromagnetic device optimization," *IEEE Trans. Magn.*, vol. 40, no. 2, pp. 1196–1199, Mar. 2004.

So-Yeon Im received the bachelor's degree in automotive engineering, in 2020 from Hanyang University, Seoul, South Korea, where she is currently working toward the Ph.D. degree in automotive engineering. Her research interests include the optimization, design, and system modeling of electric vehicles.

Tae-Gun Lee received the bachelor's degree in mechanical engineering from Yeungnam University, Daegu, South Korea, in 2021, and the master's degree in automotive engineering from Hanyang University, Seoul, South Korea, in 2023. His research interests include the design and analysis of electric machines considering electromagnetics and multi-physics required for various industries, such as home appliances and automotive.

Ki-Won Kim received the bachelor's degree in control & instrumentational engineering from Korea University, Sejong, South Korea, in 2021, and the master's degree in automotive engineering from Hanynag University, Seoul, South Korea, in 2023. Since 2023, he has been an Engineer with HD-Hyundai Electirc, Bundang, South Korea. His research interests include electromagnetic field analysis and thermal analysis through lumped parameter thermal network for motor.

Jin-Cheol Park received the bachelor's degree in electrical engineering from Chungbuk University, Cheongju, South Korea, in 2015, and the master's and Ph.D. degrees in automotive engineering from the Hanyang University, Seoul, South Korea, in 2017 and 2022, respectively. Since 2022, he has been a Specialist Researcher of Samsung Research Robot Team, Samsung Electronics. His main research interests include electric machine design for automotive and numerical analysis of electromagnetic.

Jun-Woo Chin received the bachelor's degree in mechanical engineering from Hanyang University, Seoul, South Korea, in 2014, and the integrated master's and Ph.D. degree in automotive engineering from Hanyang University, Seoul, in 2022. Since 2022, he has been with Eco-friendly Vehicle R&D Division of Korea Automotive Technology Institute, Cheonan, South Korea, where he is currently a Senior Engineer. His research interests include electromagnetic field loss, multi-physics analysis of electric machines, and their design optimization considering systems, such as automotive application.

Myung-Seop Lim (Senior Member, IEEE) received the bachelor's degree in mechanical engineering and the Master's and Ph.D. degrees in automotive engineering from Hanyang University, Seoul, South Korea, in 2012, 2014, and 2017, respectively. From 2017 to 2018, he was a Research Engineer with Hyundai Mobis, Yongin, South Korea. From 2018 to 2019, he was an Assistant Professor with Yeungnam University, Daegu, South Korea. Since 2019, he has been with Hanyang University, Seoul, where he is currently an Assistant Professor. His research interests include electromagnetic field analysis and multi-physics analysis of electric machinery for mechatronics system, such as automotive and robot applications.